https://doi.org/10.15407/ufm.24.04.741

P.E. MARKOVSKY [1,*], D.V. KOVALCHUK [1,2], J. JANISZEWSKI [3], B. FIKUS [3,], D.G. SAVVAKIN [1,***], O.O. STASIUK [1], D.V. ORYSHYCH [1], M.A. SKORYK [1], V.I. NEVMERZHYTSKYI [1,2], and V.I. BONDARCHUK [1]**

[1] G.V. Kurdyumov Institute for Metal Physics of the N.A.S. of Ukraine, 36, Acad. Vernadsky Boulevard, UA-03142 Kyiv, Ukraine
[2] JSC NVO 'Chervona Hvylya', 28 Dubrovitska Str., UA-04114 Kyiv, Ukraine
[3] General Jarosław Dąbrowski Military University of Technology, 2 General Sylwester Kaliski Str., PL-00-908 Warsaw, Poland

* pmark@imp.kiev.ua, ** bartosz.fikus@wat.edu.pl, *** savva@imp.kiev.ua

NEW APPROACH FOR MANUFACTURING TI–6AL–4V + 40%TIC METAL-MATRIX COMPOSITES BY 3*D* PRINTING USING CONIC ELECTRON BEAM AND CORED WIRE. PT. 2: LAYERED MMC/ALLOY MATERIALS, THEIR MAIN CHARACTERISTICS, AND POSSIBLE APPLICATION AS BALLISTIC RESISTANT MATERIALS

Bilayer samples comprised of hard metal-matrix composite top layer and ductile 10 mm Ti–6Al–4V plate are produced with 3D printing by conical electron-beam method using specially prepared core (powder) wire that allows forming hard top layer of metal-matrix (Ti–6Al–4V) composite (MMC) reinforced by means of fine TiC particles with thickness up to 4 mm. Ballistic tests performed with 7.62′51 AP ammunition show a good ballistic resistance of this protective structure, *i.e.*, it is not perforated. Only minor penetration and partial fracture are occurred exclusively

Citation: P.E. Markovsky, D.V. Kovalchuk, J. Janiszewski, B. Fikus, D.G. Savvakin, O.O. Stasiuk, D.V. Oryshych, M.A. Skoryk, V.I. Nevmerzhytskyi, and V.I. Bondarchuk, New Approach for Manufacturing Ti–6Al–4V + 40% TiC Metal-Matrix Composites by 3*D* Printing Using Conic Electron Beam and Cored Wire. Pt. 2: Layered MMC/Alloy Materials, Their Main Characteristics, and Possible Application as Ballistic Resistant Materials, *Progress in Physics of Metals*, **24**, No. 4: 741–763 (2023)

in the surface MMC layer. Either no traces of plastic deformation are found at the boundary with the base layer or inside it that indicates that the MMC layer absorbs the entire impact energy of the projectile. Based on studies of the fine structure and texture of the interface between the layers, a reasonable assumption is made that wavy geometry of MMC layer provides additional deflection and scattering of stress waves generated during impact. Comparing the results of ballistic tests of various metallic materials, it is concluded that the 3D-printed bilayer material consisting of the upper Ti–6Al–4V + 40% TiC layer and the base Ti–6Al–4V layer has an undeniable advantage in ballistic performance when it is tested with cartridges of this type.

Keywords: additive manufacturing, 3*D* printing, titanium alloys, metal-matrix composite, microstructure, texture, ballistic performance.

1. Introduction

As has already been shown in a large number of works, 3*D*-printing techniques make it possible to create a wide range of products from titanium alloys [1–11]. This also applies to a variant of this technology such as additive manufacturing using a conically converging electron beam and wire as a feedstock material [8, 12, 13]. This approach allows not only producing complicated net-shape products [8, 14], but also manufacturing multilayer materials with gradient composition, microstructure and, accordingly, unique properties [15]. As it was shown in some previous studies, production of layer structures allows solving a serious problem typical for titanium alloys, namely, relatively low hardness and low wear resistance [16]. It has previously been shown [15] that titanium-based layered and/or gradient materials combining harder surface and ductile bulk can be effectively used as protective armour elements with high resistance against damage even with armour-piercing bullets [17]. However, the use of conventional manufacturing powder approaches such as blended elemental powder metallurgy (BEPM [18, 19]), including additional treatment of sintered powder compacts by hot isostatic pressing [20], has a number of limitations due to limited capabilities of pressing equipment, the need to manufacture expensive moulds and other devices for each individual type of product, *etc*. In turn, the method of 3*D* printing with electron beam and wire as feedstock material is much more flexible and productive one [7, 8, 12, 13]. As shown in our previous study (see Pt. 1 [21]), the manufacturing of a special cored wire containing a mixture of powders to achieve the target Ti–6Al–4V + 40 vol.% TiC composition allowed production of bilayer material where the hardened top layer of the corresponding metal-matrix composite (MMC) was built up on ductile wrought Ti–6Al–4V alloy plate as a substrate. This second part is devoted to technology producing bilayer semi-finished products that can be used as elements of antiballistic armour and the evaluation of their protective characteristics.

2. Features of Bilayer Material with 3*D*-Printed MMC Top Layer

2.1. Manufacturing the Samples

Two similar samples consisting of Ti–6Al–4V alloy plate as a substrate and 3*D* printed MMC Ti–6Al–4V+40% TiC top layer (Figs. 1, *a*, *c*) were studied. Both samples were manufactured using similar protocols, and, hence, did not noticeably differ from each other in order to provide better statistics upon ballistic testing. The samples were produced by JSC NVO 'Chervona Hvylya' company with conical electron-beam ('X-Beam® 3*D* printing') method using cored (powder) wire as it is described in our previous work (Pt. 1 [21]). The additive manufacturing process (3*D* Printing) was performed on the industrial scale installation xBeam-Grand-1 designed and produced by JSC NVO 'Chervona Hvylya' (Fig. 2, *a*).

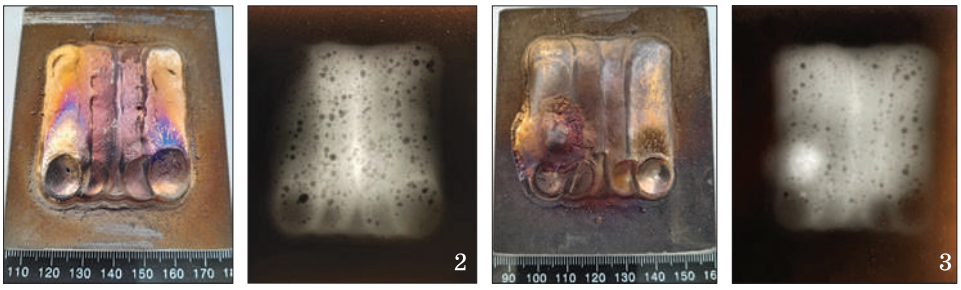

a *b* *c* *d*

Fig. 1. General view (*a*, *c*) and x-ray defectoscopy images (*b*, *d*) of samples #1 (*a*, *b*) and #2 (*c*, *d*)

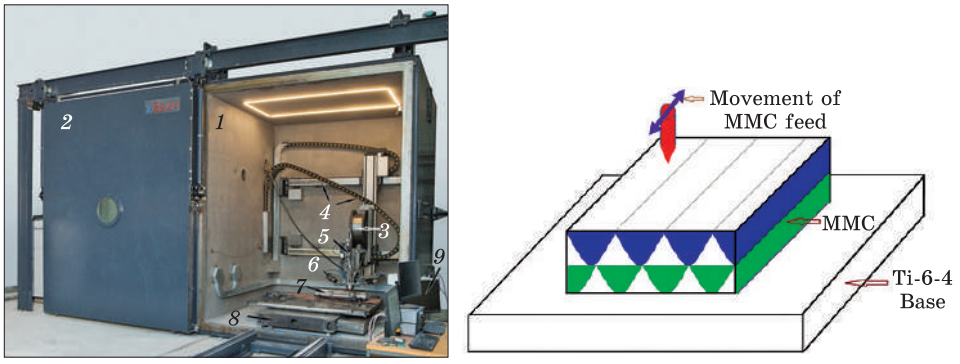

a *b*

Fig. 2. Industrial 3*D*-printing system xBeamGrand-1 at 'Chervona Hvylya' facilities, using which the samples were manufactured additively. The numbers indicate: #1 — the internal part of the vacuum chamber, #2 — opened chamber door, #3 — coil with wire, #4 — system of 3*D*-moving and voltage supple to the electron beam gun, #5 — wire feeding system with and electron beam gun at the bottom, #6 — control video camera, #7 — object being printed, #8 — 2*D* moving table, #9 — control equipment. (*b*) scheme of "shift" strategy of 3*D*-printing of the top MMC layer

MMC layer 3.5–4 mm in thickness was printed with 5–6 passes using so called 'shift printing strategy' (Fig. 2, *b*), which earlier demonstrated better balance of mechanical properties for 3*D*-printed alloy products, when commercial Ti–6Al–4V wire was employed [13, 22]. The Ti–6Al–4V plates of 10 mm thick (produced by TIMET, USA) were used as base material (substrate) for 3*D* printing. As clearly seen from Figs. 1, *a* and *b*, the printed MMC layers have somewhat wavy surfaces, that can be useful in terms of projectile deflection upon impact. X-ray defectoscopy of the 3*D* printed top layers showed their fairly dense state; however, some pores up to 1.7 mm in diameter were observed (dark spots in Figs. 1, *b*, *d*). Average hardness of the printed MMC layers was not less than 800 *HV*, while the hardness of Ti–6Al–4V base was 330×15 *HV*. Dimensions of both samples were about 85×90×10 mm, weight was about 40±7 g.

2.2. Ballistic Tests

The tests were performed at the Ballistic Test Laboratory of Military University of Technology using the experimental stand shown in Figs. 3, *a*–*c*. The 7.62×51 AP ammunitions [23] (NATO standard, produced by MESKO S.A., Poland) were used (Figs. 3, *d*, *e*) to determine of ballistic resistance of the tested protective structure. Main characteristics of the cartridges are listed in Table 1. It should be noted the high hardness (870 *HV*) and the special shape of the cores (see blunt front end in Fig. 3, *e*) designed to enhance the plugging effect and reduce the core ricochets for slightly oblique impacts. The target samples were mounted in a special holder, which was adapted to mounting relatively small target samples. The shooting was carried out from a ballistic barrel, the axis of which was oriented perpendicularly to the target, with a target position uncertainty of ±2%, whereas the projectile velocity was determined with a measurement uncertainty of ±0.3%. The holder and target samples were placed inside a protective box, which limited the spread of fragments and possible damage to the measuring equipment. The protective box also had two viewing windows, thanks to which it was possible to illuminate the front surface of the target and optical observation using a monochromatic high-speed camera.

One shot was fired into each sample, the front surface of which with the MMC layer was directed towards the bullet impact. Based on measured bullets' velocities (V), the kinetic energies values (E_k) were calcu-

Table 1. **The main characteristics of the cartridges used**

Type	Total weight, g	Core weight, g	Core diameter, mm	Core nose angle, degree	Core material	Core hardness, *HV*
7.62×51 mm AP	9.45	4.4	5.6 (rear part)/ 5.4 (front part)	45 (flat nose)	hardened steel	870

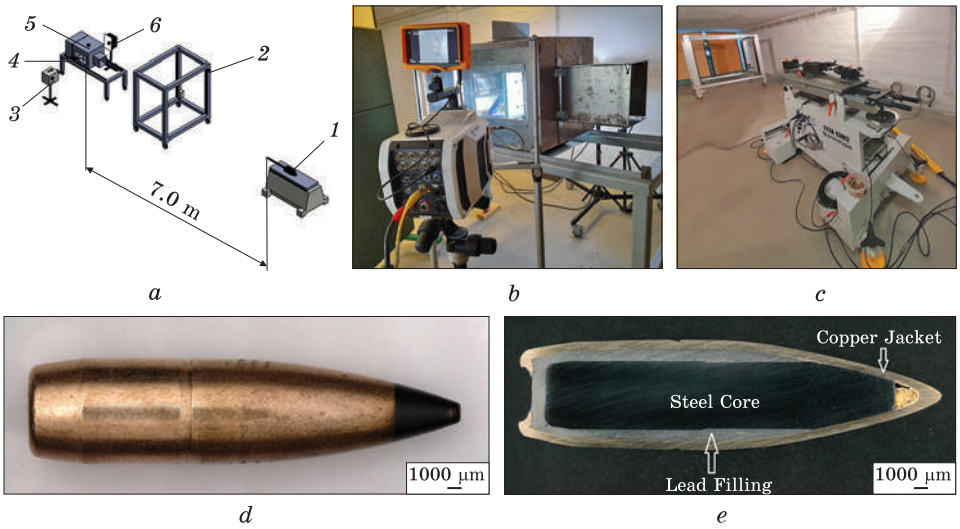

Fig. 3. (*a*) Scheme and (*b–c*) general views of the stand for ballistic tests; (*d*) general view of 7.62×51 mm AP bullet, and (*e*) its longitudinal section. Desig-nations in (*a*): #1 — mobile firing rest STZA 13M2 equipped with ballistic barrel (*b*); #2 — projectile velocity measurement light screen Kistler 2521A; #3 — high speed camera Phantom v1612 (*c*); #4 and #5 — sample mount with anti-debris protective cover, armoured glass window, and bullet catcher (*c*); #6 — LED light source

lated, which were as follow: V = 845 m/s, E_k = 3374 J for the sample #1, and V = 839 m/s, E_k = 3326 J for the sample #2.

3. Detailed Study of the Fracture and Microstructure of Tested Samples

3.1. Surface Effects Observed in the Tested Samples

Visual results of ballistic tests are presented in Fig. 4. Both samples demonstrated very similar results, which allowed determining the general behaviour of binary-layered MMC/alloy materials under ballistic impact. It is clearly seen, that samples were not pierced (Figs. 4, *a* and *d*), being damaged mainly within the surface (front) MMC layer; the crater depth in both cases did not exceed 2.6 mm (Figs. 4, *b* and *e*). No signs of plastic deformation were observed on the reverse side of the plates (Figs. 4, *c* and *f*). The upper part of MMC layer was delaminated, and fractured surfaces were located exclusively within the MMC layer being nearly perpendicular to the direction of bullet impact (Figs. 4, *b* and *e*). The cracks partly propagated along the 'tracks' of 3*D* printing (Figs. 4, *a*, *b*, *d*, and *e*). Similar effect of cracking along the printing tracks was observed also in Ref. [24]. These facts suggest the predominant role of 3*D*-printed MMC layer for dissipation of the impact energy and stopping the bullet. Taking into account the probable distribution of dis-

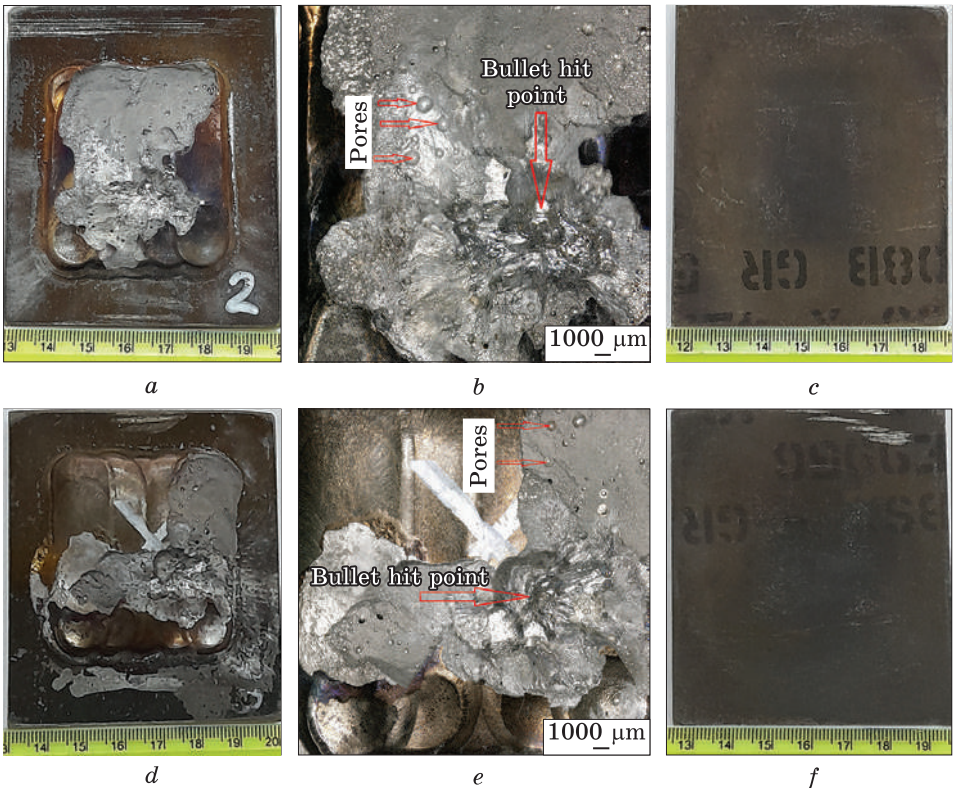

Fig. 4. Samples #1 (*a*–*c*) and #2 (*d*–*f*) after ballistic tests: front (*a*, *b*, *d*, *e*) and rear (*c*, *f*) views; *b* and *e* — digital LM

placement and energy in compressive, shear, and Rayleigh waves arising in the material under shock loading [25, 26], it can be assumed that shock waves might be reflected from the interface between the MMC layer and Ti–6Al–4V base with their predominant redirection and propagation in the plane parallel to the surface of the samples.

More detailed SEM study of the surface of tested samples (Fig. 5) showed that the impact craters on both samples contained traces of melting and splashes of lead. In addition, characteristic feature is the presence of both brittle cleavage surfaces and relatively ductile fractured surfaces. A number of 'opened' pores were observed on the fracture surfaces (Figs. 5, *a*, *b*), suggesting that main cracks propagated during their growth from one pore to another nearby one. Individual cracks seem to propagate along the boundaries between the MMC printed 'beans' formed during repeated layer-by-layer passes (Fig. 5, *c*). In some locations (in bullet impact point), chipping of individual microvolumes took place (Fig. 5, *b*). At the same time, separate small secondary cracks can be observed going deeply into the MMC layer (Fig. 5, *b*).

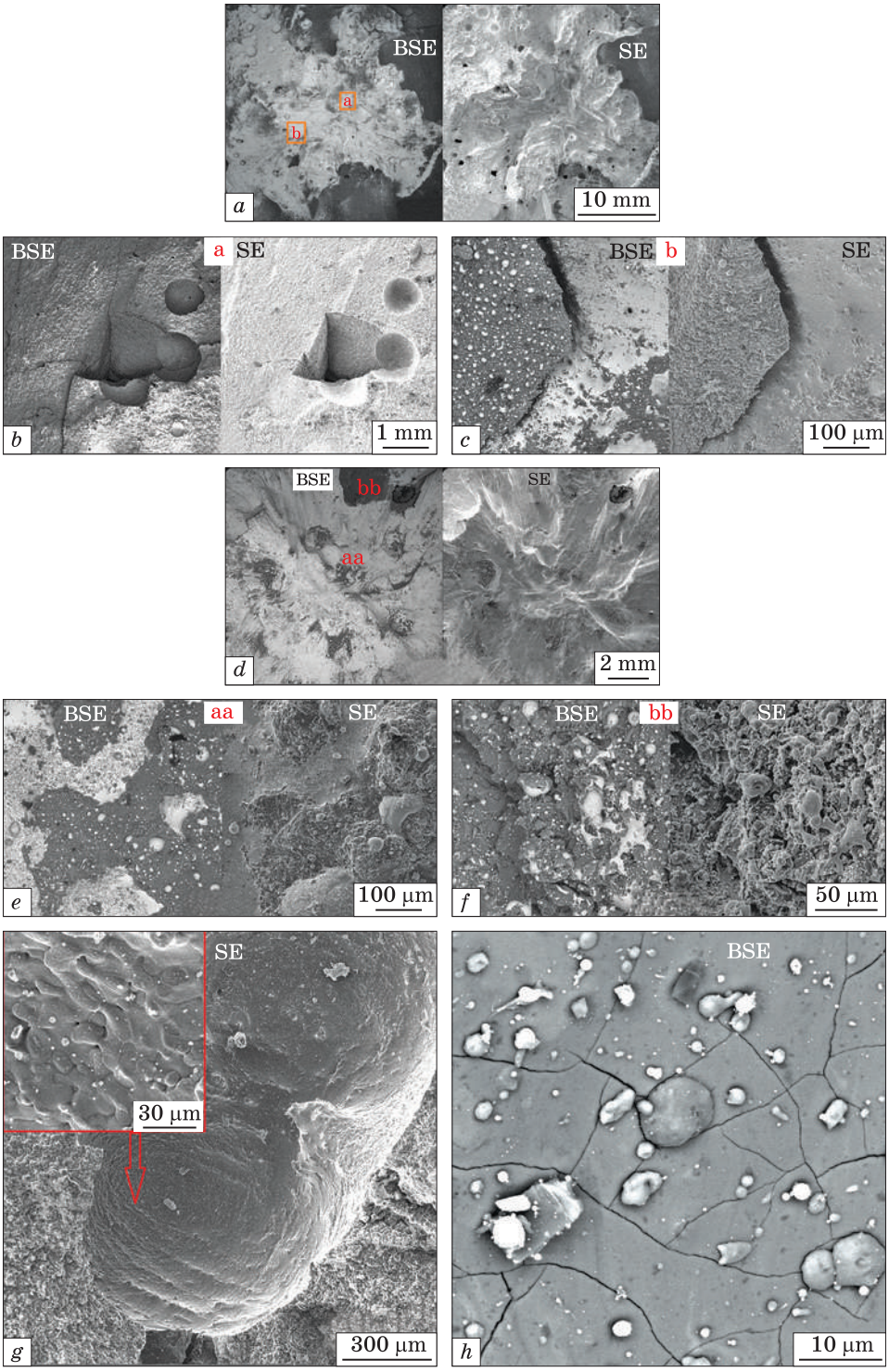

Fig. 5. SEM images of craters formed by bullets' impact in the samples (*a*–*c*) #2, and (*d*–*h*) #3; *b* and *c* — relevant images shown in *a*; *e* and *f* — in *d*; *g* — typical pore; *h* — high resolution image of 'flat' cleavage zone at the distance of 2 cm from bullet hit point

More detailed investigation revealed inside the bullet impact point both flat and rather ductile, as well as brittle areas (Fig. 5, *e*). As the main crack propagated, zones of brittle fracture formed in separate locations; obviously, these zones had either higher concentration of TiC particles, or specific crystallographic orientation (Fig. 5, *f*). As for the internal structure of the pores, they had a specific layered inner surface, which, at higher magnification, contains facets that may correspond to individual grains (Fig. 5, *g*). Despite the fact that pores are potential stress concentrators and weak structural links, no particular influence of pores on the nucleation of new cracks during fracture was found. Most likely, the harmful role of the pores as weak structural links was mitigated because, as was suggested above, the growing cracks simply propagated from a pore to the nearest one along the 'path of least resistance'. It should also be noted that the networks of small secondary cracks were observed on the flat ductile fracture surfaces at higher magnifications (Fig. 5, *h*), which, obviously, reflects the grain boundaries in the Ti–6Al–4V matrix.

3.2. Crater Cross-Section Studies

Interesting information was obtained when studying the microstructure of the cross section cut through the crater from the bullet impact (Fig. 6). Figure 6, *a* represents the general view of the central part of vertical cross-section cut through the centre of the crater made by a bullet. First of all, attention should be paid to the asymmetric shape of the crater, cracks in the upper 3*D*-printed MMC layer, and a wavy interface between the printed MMC and base alloy layers. Several quite coarse (up to 0.8 mm) pores are also seen in the cut plane. The bottom of the crater is flat, which is most likely due to the peculiarity of the used AP bullets with a blunt tip of the armour-piercing core (see Fig. 3, *e*).

A microstructure study at higher resolution (Fig. 6, *b*) and the distribution of chemical elements (Fig. 6, *c*) showed the following features. The main crack nucleated from the edge of the flat 'bottom' of the crater and propagated into the hard MMC layer, initially at an angle of about 45°, and stopped at a more plastic area depleted of TiC particles. At the same time, microstructure analysis (circled in Fig. 6, *b*) suggests this crack 'cuts' with a shift a micro-volume depleted of carbides but somewhat enriched by aluminium and vanadium (Fig. 6, *c*). Microstructure details of different locations in relation to the general cross-section view (Fig. 7, *a*) are shown in Fig. 7, *b*–*h*.

The cracks nucleated on the crater surface and propagated into the material, deviating from straight path on the clusters of fine TiC particles (Fig. 7, *b*). Similar behaviour was observed for the cracks that nucleated on the side surface (Fig. 7, *b*) and bottom of the crater (Fig. 7, *d*).

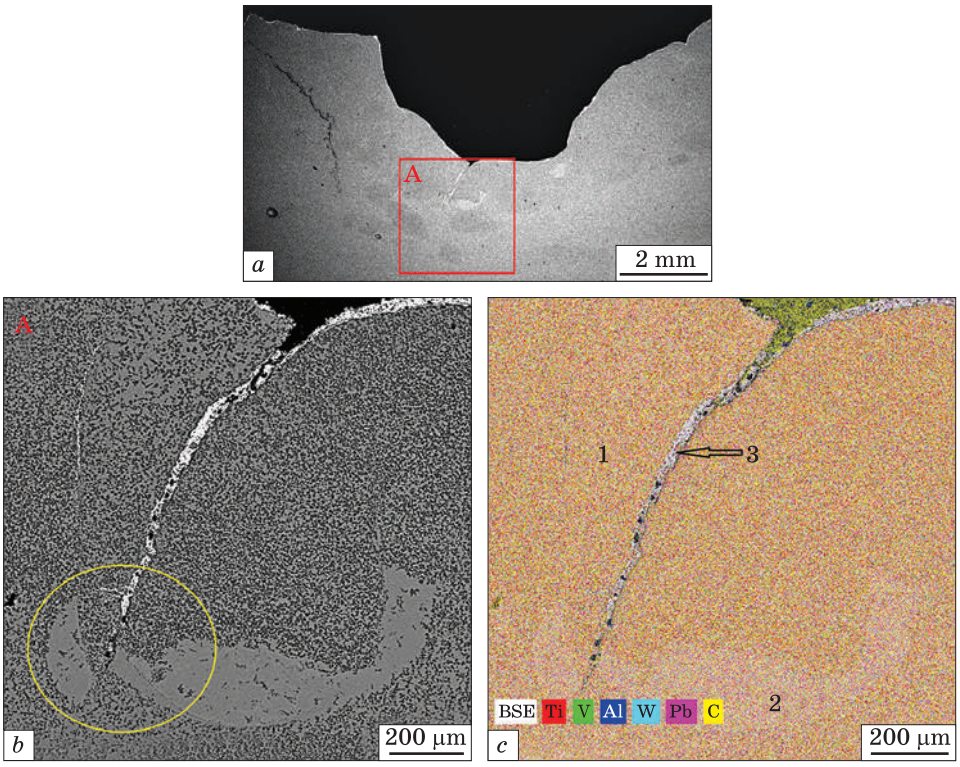

Fig. 6. Cross-section of the ballistic tested sample showing general view of the crater (*a*), analysed region (*A*) around the crack (*b*), and distribution of chemical elements (EDS analysis) in this zone (*c*). Areas in (*c*): *1* — uniformly distributed all alloying elements and fine TiC particles, *2* — zone depleted of TiC particles and enriched by Ti and Al, *3* — crack filled with molten lead. SEM, BSE

When crack propagated through the matrix and encountered TiC particles (denoted as *1* in Fig. 7, *c*), it branched to neighbouring particles (marked as *2*, *3*, and *4* in Fig. 7, *c*), that resulted in intensive cracking of the particles. As can be clearly seen in Fig. 7, *c* and *d*, the propagating crack passed through the hard TiC particles and fractured them with noticeable energy losses.

However, no traces of plastic deformation or fracture were found close to the interface between the MMC layer and the Ti–6Al–4V base layer even under the crater (Fig. 7, *e*). Partial transformation of the original equiaxed microstructure of the wrought Ti–6Al–4V plate (Fig. 7, *f*) into a coarse-grained lamellar one was observed in the heat affected zone (HAZ) of 3*D*-printing process (area *d* in Fig. 7, *e*), while equiaxed structure was preserved at the distance less than about 2 mm from MMC/alloy interface (zone *e* in Fig. 7, *f*).

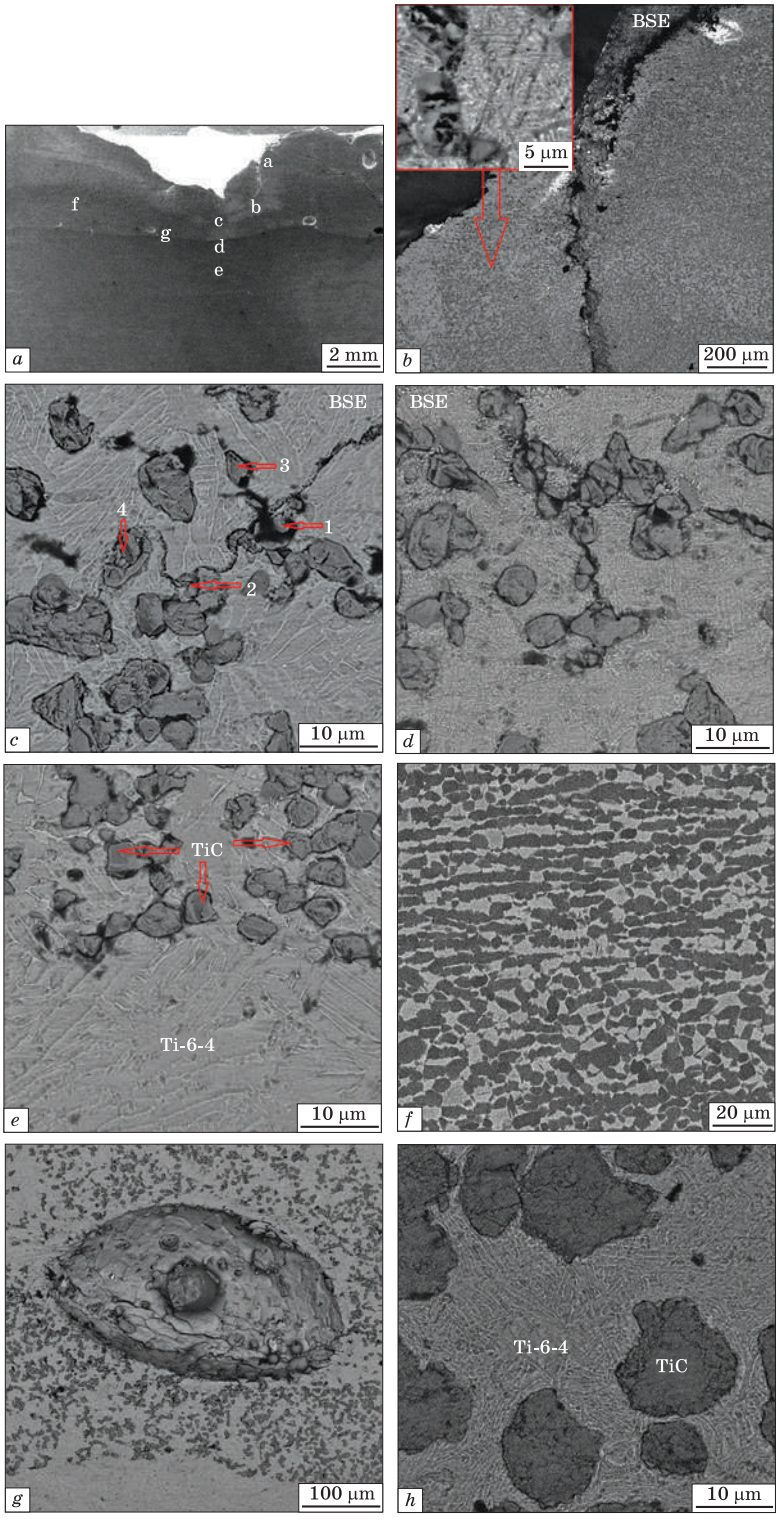

Fig. 7. Typical microstructure of the cross-section cut through the centre of crater: (*a*) general view with indicated zones investigated in detail (*b*–*h*). SEM, BSE

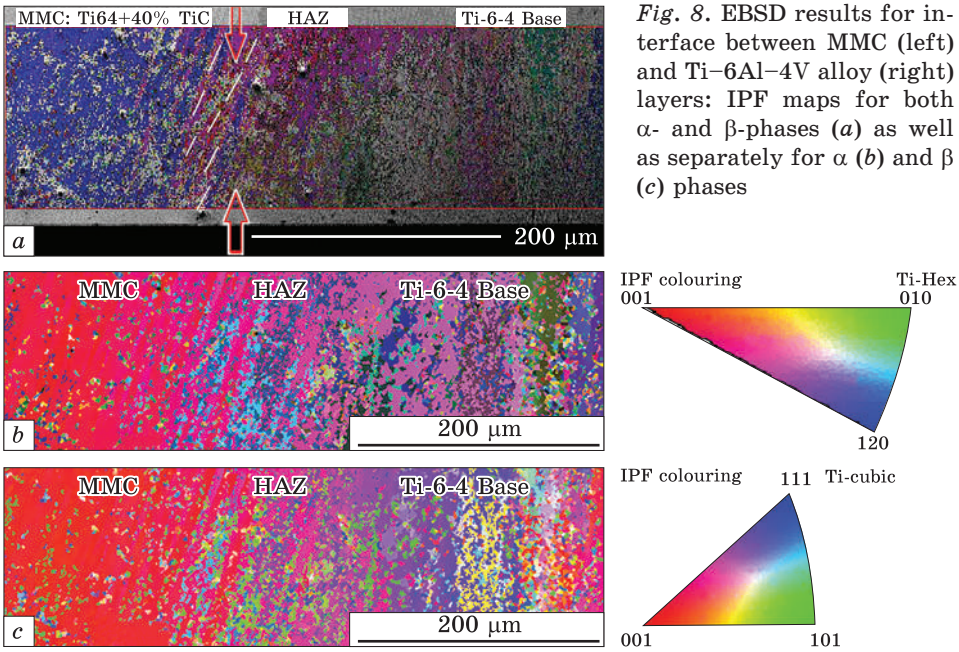

Fig. 8. EBSD results for interface between MMC (left) and Ti–6Al–4V alloy (right) layers: IPF maps for both α- and β-phases (*a*) as well as separately for α (*b*) and β (*c*) phases

Besides, we can note the deformation behaviour (partial flattening under the bullet impact) of the pores located under the crater at some distance from its centre (region *g* in Fig. 7, *g*). The traces of plastic deformation and cracking are observed at inner surface of pore along the grain boundaries of the matrix alloy.

In order to delve deeper into the physical nature of the possible interaction of shock waves at the interface between the 3*D*-printed MMC layer and the Ti–6Al–4V base plate, the features of the crystallographic texture near this interface were studied (Fig. 8). As seen, the boundary between MMC and Ti–6Al–4V platelayers (shown by arrows in Fig. 8, *a*) is not flat and has a slight slope (shown by white dashed lines) in some zones. The IPF maps in Figs. 8, *b* and *c* allow us to conclude that both α- and β-phase in the MMC layer have predominant (001) orientation. At the interface where the 3*D*-printed MMC layer was fused with the Ti–6Al–4V alloy base layer, there is a rather gradual local change of (001) orientation towards (120) and (111) for the α (Fig. 8, *b*) and β (Fig. 8, *c*) phases, respectively. Within the heat affected zone (HAZ), the random distribution of local crystallographic orientations similar to that typical for fine-grained structure of rolled Ti–6–4 plate is observed (right edges of IPF maps in Figs. 8, *b* and *c*). Thus, summing up the data on the microstructure (Fig. 7) and microtexture (Fig. 8) of the interface and transition zone between the layers, we can conclude that the boundary between the upper MMC layer and the bottom alloy layer has

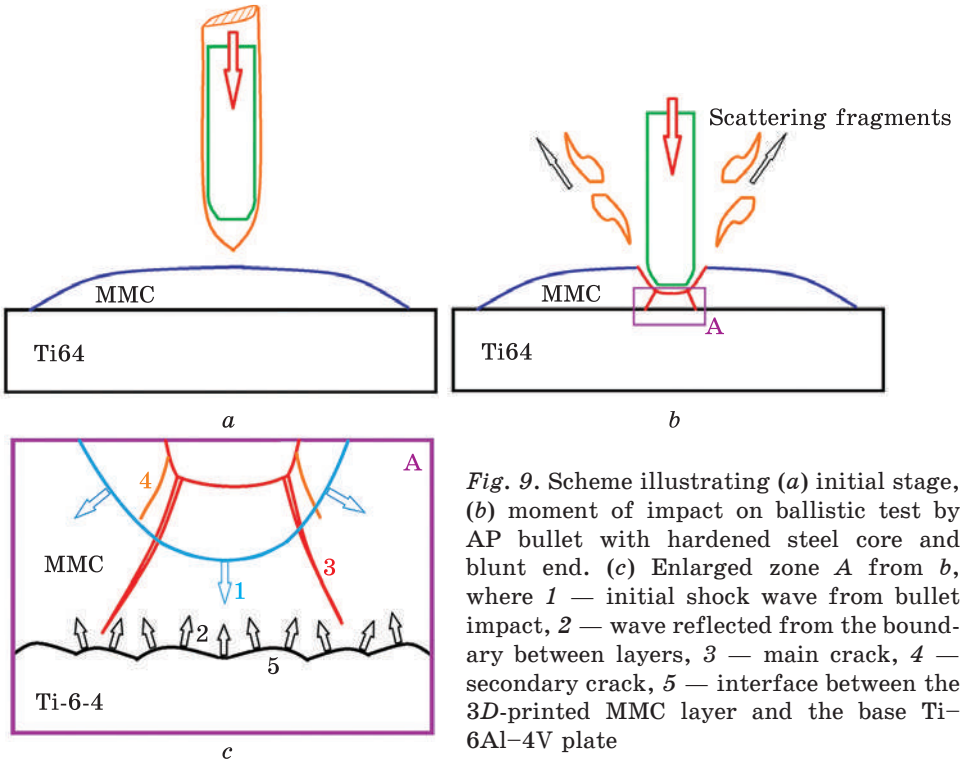

Fig. 9. Scheme illustrating (*a*) initial stage, (*b*) moment of impact on ballistic test by AP bullet with hardened steel core and blunt end. (*c*) Enlarged zone *A* from *b*, where *1* — initial shock wave from bullet impact, *2* — wave reflected from the boundary between layers, *3* — main crack, *4* — secondary crack, *5* — interface between the 3*D*-printed MMC layer and the base Ti–6Al–4V plate

a wavy shape and complex structure; this can promote reflection of shock waves and dissipation of energy of projectile impact.

In addition to above, it can be noted that during dynamic tests performed by the split Hopkinson pressure bars (SHPB) method on similar bilayer samples comprised of two layers, MMC and Ti–6Al–4V plate, cracks always formed in the hard particle-reinforced MMC layer regardless of which specimen side the impact of the input bar fell on [27]. When the crack reached the interface with the particle-free alloy layer under certain loads, it could be reflected back. It was shown by numerical simulation [26] that this phenomenon is a consequence of the specific distribution of stresses in two-layer material under dynamic loading conditions.

Results of ballistic tests and microstructure investigations can be summarized with following scheme (Fig. 9). The impact effect from the hardened steel core with a blunt end of an armour-piercing bullet 7.62×51 AP (Fig. 9, *a*) penetrates to a certain depth, forming zones of greatest localized stress diverging into the sample depth at an angle of about 45° from the edges of the flat tip (Fig. 9, *b*) in accordance with Schmid's law. The main cracks form in corresponding microvolumes (Fig. 9, *b* and *3* in Fig. 9, *c*). However, these cracks completely stop inside the MMC layer due to combined effect of hard carbides and com-

paratively ductile matrix, and do not penetrate into the alloy layer. Based on the above SEM (Fig. 7, *e*) and EBSD (Fig. 8) data, it can be assumed that initial shock wave was created as a result of the bullet hitting (*1* in Fig. 9, *c*), propagating divergently inside the MMC layer, reaching the wavy interface with the base Ti–6Al–4V alloy layer (*5* in Fig. 9, *c*), and was reflected from it at various angles (*2* in Fig. 9, *c*).

Thus, the efficiency of the anti-ballistic resistance of such a bilayer material that combines upper 3*D*-printed hard MMC Ti–6Al–4V+40% TiC layer with a ductile base layer of rolled Ti–6Al–4V plate is provided by several concurrent factors:

- high hardness of MMC due to fine high-modulus TiC particles distributed in titanium alloy matrix, comparable to the hardness of steel core of AP bullets;
- complex wavy shape and crystallographic texture of interface between the layers, which reflects and partially dissipates the shock wave;
- the base Ti–6Al–4V layer, due to its good balance of strength and ductility, plays the role of 'support' for the entire structure of the material under severe conditions of ballistic impact of a hard projectile.

4. Comparison with Other Ti-Based Materials

First of all, it is interesting to compare the above results of ballistic tests with available in the literature data by different authors conducting the tests with the use of the similar type of ammunition. More detailed study was performed by J. Fanning [28, 29] specifically for cartridges 7.62×51 AP M2 (Fig. 10). In this detailed study, V_{50} ballistic limit values for the number of titanium alloys investigated follow a straight line, with the exception of two high-strength alloys VST 3553 and TIMETAL-LCB, which, obviously, have too low ductility in strengthened (STA) state. Nevertheless, the author found out a direct dependence of V_{50} parameter *versus* the thickness of tested plates for the Ti–6Al–4V alloy. In order to compare our 3*D*-printed material with data available in literature, we also tested 14 mm thick Ti–6Al–4V plate (produced by TIMET, USA) with the similar ammunition (similar pro-

Table 2. **Results of 14 mm thick Ti–6Al–4V plate ballistic tests with 7.62×51 AP ammunition**

Shot #	*V*, m/s	*E*, J	Result	Crater depth, mm	Shot #	*V*, m/s	*E*, J	Result	Crater depth, mm
1	827	3232	Not pierced	4.3	3	836	3302	Not pierced	4.8
2	859	3486	Not pierced	5.8	4	850	3414	Pierced	{14}

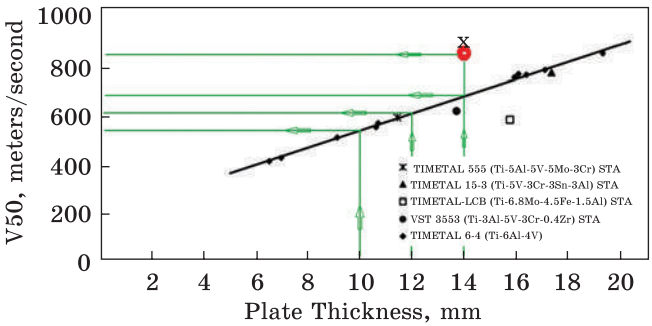

Fig. 10. Comparison of ballistic test results for various titanium alloys shot by 7.62×5.41 mm AP ammunition. V_{50} dependence is adopted from [27, 28]

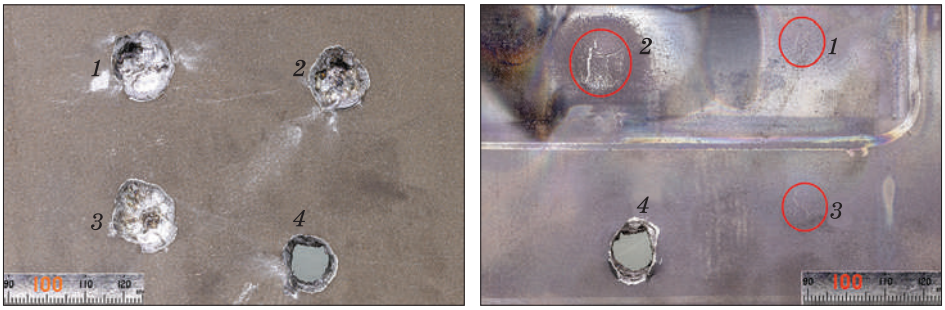

a *b*

Fig. 11. The 14 mm thick Ti–6Al–4V plate shot with 7.62×51 AP ammunition

jectile diameter, mass and core material, but different nose shape). Our tests of standard commercial 14 mm rolled Ti–6Al–4V alloy product showed V_{50} value significantly higher (point *X* in Fig. 10) than that obtained in [28, 29]. Some details of our tests are presented in Fig. 11 and Table 2 and are discussed below. The base 10 mm thick Ti–6Al–4V plate used in our experiments, according to Fanning's data, should have the V_{50} value of no more than 550 m/s (shown by green lines with arrows in Fig. 10). The plates of the same alloy with a thickness of 12–14 mm (which approximately correspond to the total thickness of our bilayer 3*D*-printed samples) should have V_{50} values about 610–690 m/s. However, our bilayer material was not pierced at higher bullet velocities (839–845 m/s), and did not have visible signs of deformation of the Ti–6Al–4V base layer! It can be the effect of different core nose shapes in case of MESKO AP and AP2 projectiles. As can be noticed in reports, the hard steel material is sensitive to this aspect. Less sensitivity is observed in case of ceramics faces and mild steel plates. This issue will be additionally investigated for the Ti–6Al–4V alloy targets [30].

An analysis of ballistic multi-hit test results for 14 mm Ti–6Al–4V plate (Fig. 11 and Table 2) shows that the first three shots did not pierce the plate, despite shot #2 had the highest velocity and bullet kinetic energy (Table 2). The depth of craters formed after shots ##1–3 did not

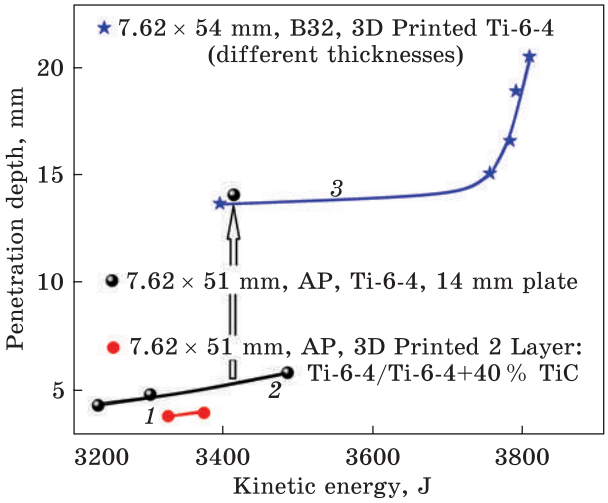

Fig. 12. Penetration depth *vs.* kinetic energy of armour piercing bullets of 7.62 mm calibre: *1* — results of the present study for bilayer MMC/Ti–6Al–4V alloy material, *2* — data for 14 mm commercial Ti–6Al–4V wrought plate, *3* — data for 3*D* printed Ti–6Al–4V samples tested with 7.62×54 mm B32 ammunition [17]

exceed 5.8 mm (Table 2, Fig. 11, *a*), while slight cracking took place on the reverse side of the plate (Fig. 11, *b*). However, shot #4 with some average bullet velocity and kinetic energy resulted in a complete piercing. It could be assumed that this result of 4th shot is not only due to some local defect of the rolled plate, but also due to stresses accumulated in the material during previous shots, so called 'ballistic fatigue', similar to fatigue observed on testing with cyclic loads [31], since a similar phenomenon was observed when testing other materials [32, 33]. This effect requires special detailed investigation.

Both these results and those previously obtained for similar former Soviet-made 7.62×54 mm B32 cartridges [17] were compared with a current 3*D*-printed bilayer material to evaluate the penetration depth of the hardened steel core of armour-piercing bullets of 7.62 calibre from different manufacturers (Fig. 12). First of all, the comparison of curves *1*, *2*, and *3* shows the smallest penetration depth of bullets for bilayer materials with top 3*D*-printed Ti–6Al–4V + 40% TiC hard layer (curve *1*), although these materials had the smallest thickness among the samples shown in the figure. For the 14 mm thick Ti–6Al–4V plate, the dependence on the bullet kinetic energy (curve *2*) is quite smooth, except for the result of the 4th shot that led to the piercing (shown by arrow). However, such a phenomenon is most likely the result of the so-called 'ballistic fatigue' of the material, which accumulates, stresses from shot to shot. The phenomenon is quite interesting and requires a special in-depth study. As for the samples 3*D* printed by the same electron-beam method using commercial Ti–6Al–4V wire (curve *3*), the penetration depth is noticeably higher than for both other materials (curves *1* and *2*). This result can be explained with somewhat higher energy of B32 cartridges, ogive-nose core of the projectile (which is closer to the 7.62 mm

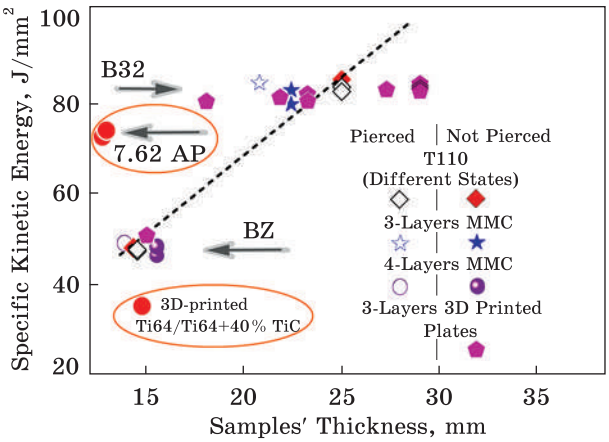

Fig. 13. Specific kinetic energy of bullets and results of ballistic tests (piercing-not piercing) depending on the thickness of titanium-based materials. All data for BZ and B32 ammunitions are adopted from [15, 17, 34]. Dashed line is plotted for the data from [28]

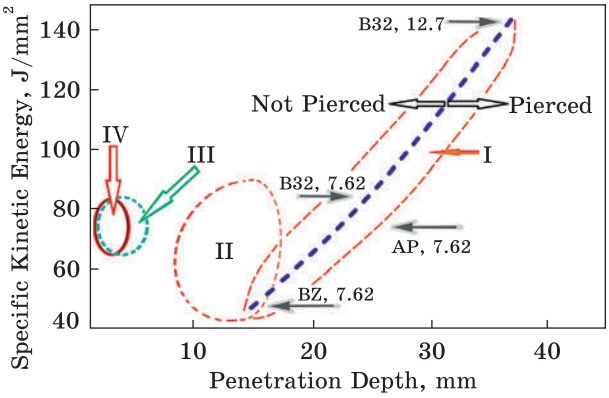

Fig. 14. Comparative diagram showing specific kinetic energy of armour-piercing bullets and penetration depth of their hardened cores into different types of titanium based materials: region *I* — rolled [17, 22, 29], and 3*D*-printed [34] titanium alloys of different compositions, area *II* — layered Ti-based materials produced by powder metallurgy approach [15, 16], and 3*D*-printing [13, 17], zone *III* — metal matrix composites reinforced by TiC or TiB particles and treated by HIP [20], and region *IV* — bilayer material tested in the present study. Dashes line within the area *I* divides this region into samples pierced and non-pierced on shooting

AP2 projectiles), as well as structural features of the 3*D*-printed bulk Ti–6Al–4V material described in [17, 33, 34].

In addition, it is important to carry out a comparative analysis of specific kinetic energy of projectiles (kinetic energy divided by cross-section area of projectiles) and their penetration depth data (Figs. 13 and 14) for different types of Ti-based materials ballistically tested by armour piercing ammunitions. Figure 13 shows general results of ballistic tests (with or without piercing) for uniform T110 alloy and layered structures combining various MMCs, Ti–6Al–4V alloy, and CP-Ti layers. These data allow approximate evaluation of armour thickness desirable for reliable protection against armour-piercing bullets. It should be emphasized once again that sufficient protecting characteristics at minimum armour thickness (Fig. 13) were demonstrated for binary-layered

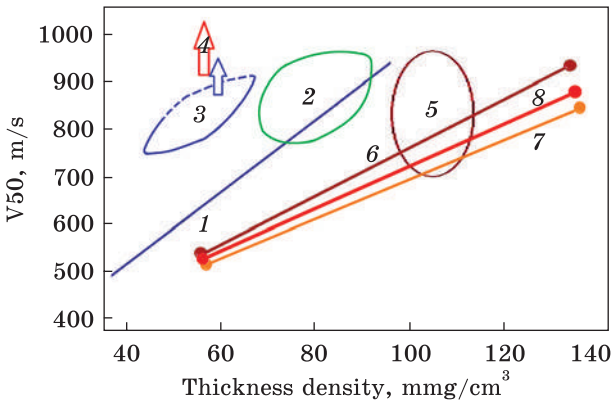

Fig. 15. Diagram showing V_{50}–thickness × material density dependencies for: *1* — various commercial rolled Ti-alloys [22, 28, 29], *2* — data for 14-mm Ti–6–4 plate (present result) and 3*D*-printed Ti–6–4 uniform materials [42], *3* — data for BEPM manufactured layered materials containing MMCs reinforced with TiC or TiB particles [34, 38], arrow shows possible position for V_{50} of MMC after HIP [20], *4* — possible position of V_{50} point for bilayer samples with 3*D*-printed MMC top layer in present study, *5*, *6* — RHA steel [38–41, 43], *7* — Aluminium 5083AL alloy [43, 45] and *8* — Magnesium AZ31B alloy [44]

3*D*-printed MMC/Ti–6Al–4V alloy armour of 10–15 mm total thickness, including the samples of present investigation. Figure 14 represents comparison for 7.62 mm [13, 15, 16, 20, 22, 29] and 12.7 mm [17, 35] calibres of AP cartridges with current results for binary 3*D*-printed MMC/Ti–6Al–4V plate material. All cast and wrought commercial titanium alloys fit well enough into the area marked as *I*; to the left from the central dotted line crossing this area, plates of the appropriate thickness were pierced, and to the right they were not pierced. 3*D*-printed titanium alloy Ti–6Al–4V studied in Ref. [17] also more or less corresponds to this area. Layered titanium materials produced with blended elemental powder metallurgy (BEPM) approach lie in the area *II* somewhat left of the area *I*, *i.e.* they have slightly greater ballistic resistance due to the combined structure comprised of hard MMCs and ductile alloy layers. The resistance of BEPM produced multilayer MMC reinforced with TiC or TiB particles becomes noticeably higher (region *III*) when hot isostatic pressing (HIP) operation is additionally involved in manufacturing process. Finally, the bilayer (3*D*-printed MMC/Ti–6Al–4V alloy plate) material studied in the present work corresponds to region *IV*, which looks the best in such comparison.

Thus, the above comparison shows that the bilayer material studied in this work is one of the most ballistically resistant among other titanium-based ones. Its characteristics are quite similar to those for MMCs based on the Ti–6Al–4V alloy matrix reinforced with 40% TiC or TiB particles manufactured by the BEPM method followed by HIP treatment. However, 3*D*-printing technology using electron beam and wire as feedstock material is more flexible, much more productive, and allows the manufacturing of products of various shapes and sizes.

The comparison of the ballistic resistance of titanium materials with conventional armour materials, like RHA steels, is of great interest. Various armour materials were compared with each other usually in terms of ballistic limit or limit velocity [36–38], for instance V_{50}, V_{90} or V_{99} [39], where the subscript numbers correspond to the percentage of projectile stopping probability. Example of such study for Ti–6Al–4V plates tested with different types of armour piercing ammunition is presented in [38]. Since in our studies piercing was achieved for a 14 mm homogeneous Ti–6Al–4V plate (Fig. 11), while in [40, 41] it was observed for Ramor 500 and Ramor 550 steels, which have 1.7 times higher density, these thicknesses correspond to V_{50} when tested with similar projectiles. Moreover, the bilayer samples tested in the present study were very far from deep penetration, what makes extremely difficult to compare obtained result with the extensive data available in the literature for other materials.

Some attempt to compare Ti-based materials with other armours was made in previous work [40] using such universal parameter as armour thickness multiplied by material density, which comparatively evaluates the weight for 1 cm^2 of armour. Based on these data and the results presented in [37, 42–44], the dependencies were plotted (Fig. 15), which take into account the specific weight of the tested materials. The following conclusions emerge from the analysis of this data:

• firstly, all titanium-based materials (indicated by *1–4*) are located to the left of all other armour metals *5–8* with equal V_{50} values, which means noticeably reduced weight of titanium-based armours with comparable protecting characteristics;

• secondly, in similar coordinates, armour steels (*5*, *6*) are not as significantly superior to magnesium (*8*) and aluminium (*7*) alloys as titanium materials (*1–4*) in ballistic performance, while magnesium alloy has better performance than aluminium;

• finally, since layered titanium-based MMCs produced with BEPM+HIP [20] and bilayer 3*D*-printed MMC/wrought Ti–6Al–4V alloy plate were not pierced (V_{50} values for them were not determined, data indicated as arrows *4* and *3*, this result suggests obvious superiority of such layered materials.

At the end of the comparative analysis of armour materials, armours based on ceramics should be also mentioned [45–47]. Such materials certainly demonstrate a good ballistic performance to weight ratio due to high hardness and kinetic energy absorption ability. However, due to the absolute fragility of such armour, it has one critical drawback: it is not able to withstand subsequent projectiles after the first defeat (low multihit resistance). This drawback is overcome by the multi-layer armour products, in which layers of different metals are combined with layers of ceramics, and some polymers [46, 47]. However, such multilayered structures are rather heavy and can be only

employed in heavy battlefield equipment. This approach was used, for example, in the 'Chobham armour' used on the Challenger 2 and M1 Abrams tanks [49].

5. Concluding Remarks

The results of ballistic tests of bilayer samples combining a Ti–6–4 plate with a 3*D* printed metal matrix composite consisting of a Ti–6–4 alloy hardened with 40% TiC particles, as well as studies on fracture and structural changes in the samples, and comparative analyses with the available data for other metallic armour materials showed the following.

• The ballistic resistance of the bilayer material has outstanding superiority over all known commercial uniform titanium rolled materials. When tested with 7.62×51 mm AP cartridges, the upper hard layer completely stops armour-piercing bullet due to scattered inclusions of TiC particles distributed within a rather ductile Ti–6–4 matrix, and moreover, there are no visible signs of damage or plastic deformation in the base Ti–6–4 layer.

• The armour resistance of such a bilayer material actually corresponds to the resistance of a pure composite of the same composition subjected to hot isostatic pressing after sintering. However, the present bilayer material is a more reliable armour material in terms of multihit scenario due to the combination with the less hard and much more ductile base plate of the Ti–6–4 alloy.

• Taking into account the specific weight, titanium alloys and titanium-based materials strengthened by dispersed hard particles have an undeniable advantage over such armour materials as RHA steels, Aluminium 5083AL alloy, and Magnesium AZ31B alloy.

• Additionally, the following advantages of producing a bilayer material using electron beam and wire 3*D*-printing technology should be emphasized, *i.e.*, flexibility in terms of the shape and dimensions of the products, as well as high productivity.

Acknowledgements. The work as a whole was carried out within the framework of two agreements on scientific and technical cooperation between G.V. Kurdyumov Institute for Metal Physics of the N.A.S. of Ukraine on the one hand and Jarosław Dąbrowski Military University of Technology along with JSC NVO 'Chervona Hvylya' on the other hand. Microstructural part of work was performed within the project 'New Metal-Containing Materials and Innovation Technologies for Priority Branches of Ukrainian Industry' (State Reg. No. 0123U100898) under the budget program КПКВК 6541230 of the National Academy of Sciences of Ukraine. Ballistic tests were co-financed by Military University of Technology in Warsaw under research projects UGB-827/2023 and UGB/22-829/2023/WAT.

REFERENCES

1. L.E. Murr, *Metallogr. Microstruct. Anal.*, **7**, No. 2: 103–132 (2018); https://doi.org/10.1007/s13632-018-0433-6
2. N. Li, S. Huang, G. Zhang, R. Qin, W. Liu, H. Xiong, G. Shi, and J. Blackburn, *J. Mater. Sci. & Technol.* **35**, No. 2: 242–269 (2019); https://doi.org/10.1016/j.jmst.2018.09.002
3. A. Bandyopadhyay and B. Heer, *Mater. Sci. Eng.*, **129**: 1–16 (2018); https://doi.org/10.1016/j.mser.2018.04.001
4. K. Markandan, R. Lim, P. Kumar Kanaujia, I. Seetoh, M.R. bin Mohd Rosdi, Z.H. Tey, J.S. Goh, Y.C. Lam, and C. Lai, *J. Mater. Sci. & Technol.*, **47**: 243–252 (2020); https://doi.org/10.1016/j.jmst.2019.12.016
5. S. Liu and Y.C. Shin, *Mater. & Des.*, **164**: 107552 (2019); https://doi.org/10.1016/j.matdes.2018.107552
6. A.R. Balachandramurthi, J. Olsson, J. Elgerdh, A. Snis, J. Moverare, and R. Pederson, *Results Mater.*, **1**, 100017 (2019); https://doi.org/10.1016/j.rinma.2019.100017
7. D.V. Kovalchuk, V.I. Melnik, I.V. Melnik, and B.A. Tugaj, *Automatic Welding*, **2017**, No. 12: 26–33 (2017); https://doi.org/10.15407/as2017.12.03
8. D. Kovalchuk, and O. Ivasishin, *Profile Electron Beam 3D Metal Printing, Additive Manufacturing for the Aerospace Industry* (Elsevier: 2019), p. 213–233; https://doi.org/10.1016/b978-0-12-814062-8.00012-1
9. M.O. Vasylyev, B.M. Mordyuk, and S.M. Voloshko, *Prog. Phys. Met.*, **24**, No. 1: 5–37 (2023); https://doi.org/10.15407/ufm.24.01.005
10. M.O. Vasylyev, B.M. Mordyuk, and S.M. Voloshko, *Prog. Phys. Met.*, **24**, No. 1: 38–74 (2023); https://doi.org/10.15407/ufm.24.01.038
11. A.V. Zavdoveev, T. Baudin, D.G. Mohan, D.L. Pakula, D.V. Vedel, and M.A. Skoryk, *Prog. Phys. Met.*, **24**, No. 3: 561–592 (2023); https://doi.org/10.15407/ufm.24.03.561
12. D. Kovalchuk, O. Ivasishin and D. Savvakin, *MATEC Web Conf.*, **321**: 03014 (2020); https://doi.org/10.1051/matecconf/202032103014
13. D. Kovalchuk, V. Melnyk, I. Melnyk, D. Savvakin, O. Dekhtyar, O. Stasiuk, and P. Markovsky, *J. Mater. Eng. Perform* **30**, No. 7: 5307–5322: (2021); https://doi.org/10.1007/s11665-021-05770-9
14. D. Kovalchuk, V. Melnyk, and I. Melnyk, *J. Mater. Eng. Perform.*, **31**, No. 8: 6069–6082 (2022); https://doi.org/10.1007/s11665-022-06994-z
15. P.E. Markovsky, D.G. Savvakin, O.O. Stasiuk, S.H. Sedov, V.A. Golub, D.V. Kovalchuk, and S.V. Prikhodko, *Metallofiz. Noveishie Tekhnol.*, **43**, No. 12: 1573–1588 (2021); https://doi.org/10.15407/mfint.43.12.1573
16. P.E. Markovsky, D.G. Savvakin, O.M. Ivasishin, V.I. Bondarchuk, and S.V. Prikhodko, *J. Mater. Eng. Perform.*, **28**, No. 9: 5772–5792 (2019); https://doi.org/10.1007/s11665-019-04263-0
17. P.E. Markovsky, O.M. Ivasishin, D.G. Savvakin, O.O. Stasiuk, V.I. Bondarchuk, D.V. Oryshych, D.V. Kovalchuk, S.H. Sedov, V.A. Golub, and V.V. Buznytskyi, *Metallofiz. Noveishie Tekhnol.*, **44**, No. 10: 1361–1375 (2022); https://doi.org/10.15407/mfint.44.10.1361

18. O.M. Ivasishin and V.S. Moxson, *Low-Cost Titanium Hydride Powder Metallurgy, Titanium Powder Metallurgy: Past, Present and Future* (New York: Elsevier: 2015), p. 117–148; https://doi.org/10.1016/B978-0-12-800054-0.00008-3
19. O.M. Ivasishin, P.E. Markovsky, D.G. Savvakin, O.O. Stasiuk, M.N. Rad, and S.V. Prikhodko, *J. Mater. Process. Technol.*, **269**: 172–181 (2019); https://doi.org/10.1016/j.jmatprotec.2019.02.006
20. P. Markovsky, J. Janiszewski, D. Savvakin, O. Stasiuk, B. Fikus, V. Samarov, and S. Prikhodko, *Materials* (2023) (in press).
21. P.E. Markovsky, D.V. Kovalchuck, S.V. Akhonin, S.L. Schwab, D.G. Savvakin, O.O. Stasiuk, D.V. Oryshych, D.V. Vedel, M.A. Skoryk, and V.P. Tkachuk, *Prog. Phys. Met.*, **24**, No. 4: 715–740 (2023); https://doi.org/10.15407/ufm.24.04.715
22. A.E. Davis, J.R. Kennedy, D. Strong, D. Kovalchuk, S. Porter, and P.B. Prangnell, *Materialia*, **20**: 101202: (2021); https://doi.org/10.1016/j.mtla.2021.101202
23. *Nammo: 7.62 mm ´51 Armor Piercing 8 (M993)*; https://www.nammo.com/product/our-products/ammunition/small-caliber-ammunition/7-62mm-series/7-62-mm-x-51-armor-piercing-8-m993/
24. I. Szachogłuchowicz, B. Fikus, K. Grzelak, J. Kluczyński, J. Torzewski, and J. Łuszczek, *Materials*, **14**, No. 10: 2681 (2021); https://doi.org/10.3390/ma14102681
25. R.D. Woods, *J. Soil Mech. Found. Div.*, **94**, No. 4: 951–979 (1968); https://doi.org/10.1061/jsfeaq.0001180
26. J.K. Lee, *Analysis of Multi-Layered Materials under High Velocity Impact Using CTH* (PhD Thesis on Master of Science in Aeronautical Engineering, Air Force Institute of Technology: 2008); https://scholar.afit.edu/etd/2685
27. P.E. Markovsky, J. Janiszewski, D.G. Savvakin, O. Stasiuk, Kamil Cieplak, P. Baranowski, and S.V. Prikhodko, *Materials & Design*, **223**: 111205–111205 (2022); https://doi.org/10.1016/j.matdes.2022.111205
28. J.C. Fanning, *J. Mater. Eng. Perform.*, **14**, No. 6: 686–690 (2005); https://doi.org/10.1361/105994905x75457
29. J. Fanning, *Proceedings of Titanium World Conference 'Titanium 99, Science and Technology'* (1999).
30. I. Horsfall, N. Ehsan, W. Bishop, *J. Battlefield Technology*, **3**: 5–8 (2000).
31. P. Peralta and C. Laird, Fatigue of Metals, *Physical Metallurgy* (Elsevier: 2014), p. 1765–1880; https://doi.org/10.1016/b978-0-444-53770-6.00018-6
32. T.L. Jones, *Ballistic Performance of Titanium Alloys: Ti–6Al–4V Versus Russian Titanium, US Army Research Laboratory Report ARL-CR-0533*, p. 19 (2004).
33. S.E. Alkhatib and T.B. Sercombe, *Mater. & Des.*, **217**: 110664 (2022); https://doi.org/10.1016/j.matdes.2022.110664
34. P.E. Markovsky, D.G. Savvakin, S.V. Prikhodko, O.O. Stasyuk, S.H. Sedov, V.A. Golub, V.A. Kurban, and E.V. Stecenko, *Metallofiz. Noveishie Tekhnol.*, **42**, No. 11: 1509–1524 (2020); https://doi.org/10.15407/mfint.42.11.1509
35. O.M. Ivasishin, P.E. Markovsky, D.G. Savvakin, O.O. Stasiuk, V.A. Golub, V.I. Mirnenko, S.H. Sedov, V.A. Kurban, and S.L. Antonyuk, *Prog. Phys. Met.*, **20**, No. 2: 285–309 (2019); https://doi.org/10.15407/ufm.20.02.285

36. D.E. Carlucci, *Ballistics: Theory and Design of Guns and Ammunition* (New York: CRC Press: 2007).
37. L. Ding, C. Li, B. Pang, and W. Zhang, *Int. J. Impact Eng.*, **35**, No. 12: 1490–1496 (2008); https://doi.org/10.1016/j.ijimpeng.2008.07.005
38. M. Walicki, J. Janiszewski, and K. Cieplak, *J. Theor. Appl. Mech.*, **60**, No. 1: 129–140 (2022); https://doi.org/10.15632/jtam-pl/144793
39. J.P.F. Broos, S.N. van Trigt, and M.C.P. Peijen, *Specialists' Meeting on Cost Effective Application of Titanium Alloys in Military Platforms, for NATO AVT Panel* (2001); https://www.researchgate.net/publication/268740375
40. M.L. Bekci, B. H. Canpolat, E. Usta, M. S. Güler та Ö.N. Cora, *Eng. Sci. Technol. Int. J.*, **24**, No. 4: 990–995 (2021); https://doi.org/10.1016/j.jestch.2021.01.001
41. *SSAB, Armox Protection Plate, Protection Steel Buildings Data Sheet*; https://ssabwebsitecdn.azureedge.net/-/media/files/en/armox/armox-protectionsteel-in-buildings-en.pdf?m=20170619110513
42. O.M. Ivasishin, D.V. Kovalchuk, P.E. Markovsky, D.G. Savvakin, O.O. Stasiuk, V.I. Bondarchuk, D.V. Oryshych, S.G. Sedov, and V.A. Golub, *Prog. Phys. Met.*, **24**, No. 1: 75–105 (2023); https://doi.org/10.15407/ufm.24.01.075
43. M.E. Backman and W. Goldsmith, *Int. J. Eng. Sci.*, **16**, No. 1: 1–99 (1978); https://doi.org/10.1016/0020-7225(78)90002-2
44. L. Jones, R.D. DeLorme, M.S. Burkins, and W.A. Gooch, *23rd Int. Symposium on Ballistics (Tarragona, Spain, 16–20 April 2007)*; https://www.researchgate.net/publication/268379604
45. B. Cheeseman, W. Gooch, and M. Burkins, *Preprint 24th Int. Ballistics Symposium (New Orleans, LA, USA, 22–26 September 2008)*; https://www.researchgate.net/publication/292393974_Ballistic_Evaluation_of_Aluminum_2139-T8
46. E. Medvedovski, *Ceram. Int.*, **36**, No. 7: 2103–2115 (2010); https://doi.org/10.1016/j.ceramint.2010.05.021
47. F. Cui, G. Wu, T. Ma, and W. Li, *Def. Sci. J.*, **67**, No. 3: 260 (2017); https://doi.org/10.14429/dsj.67.10664
48. E. Medvedovski, *Ceram. Int.*, **36**, No. 7: 2117–2127 (2010); https://doi.org/10.1016/j.ceramint.2010.05.022
49. *Chobham Armour, Wikipedia* (2022); https://en.wikipedia.org/wiki/Chobham_armour

Received 21.09.2023;
in final version, 31.10.2023

П.Є. Марковський[1], *Д.В. Ковальчук*[1,2], *Я. Янішевський*[3],
Б. Фікус[3], *Д.Г. Саввакін*[1], *О.О. Стасюк*[1], *Д.В. Оришич*[1],
М.А. Скорик[1], *В.І. Невмержицький*[1,2], *В.І. Бондарчук*[1]

[1] Інститут металофізики ім. Г.В. Курдюмова НАН України,
бульв. Академіка Вернадського, 36, 03142 Київ, Україна

[2] ПрАТ НВО «Червона хвиля»,
вул. Дубровицька, 28, 04114 Київ, Україна

[3] Військовий технологічний університет
імені Генерала Ярослава Домбровського,
вул. Генерала Сильвестра Каліського, 2, 00-908, Варшава, Польща

НОВИЙ ПІДХІД ДО ВИГОТОВЛЕННЯ МЕТАЛОМАТРИЧНИХ КОМПОЗИТІВ Ti–6Al–4V + 40% TiC 3*D*-ДРУКОМ ІЗ ВИКОРИСТАННЯМ КОНІЧНОГО ЕЛЕКТРОННОГО ПРОМЕНЯ ТА ПОРОШКОВОГО ДРОТУ. Ч. 2: БАГАТОШАРОВІ МАТЕРІАЛИ ММК/СТОПИ, ЇХНІ ОСНОВНІ ХАРАКТЕРИСТИКИ ТА МОЖЛИВЕ ЗАСТОСУВАННЯ ЯК БАЛІСТИЧНО СТІЙКИХ МАТЕРІАЛІВ

Двошарові зразки, що складалися з твердого верхнього шару металоматричного композиту та пластичної 10 мм-пластини Ti–6Al–4V, було виготовлено за допомогою методу 3*D*-друку конічним електронним променем з використанням спеціяльно підготовленого порошкового дроту. Це дало змогу сформувати твердий верхній шар композиту (ММК), який складається з металевої матриці (Ti–6Al–4V), армованої дрібними частинками TiC розміром до 4 мкм. Балістичні випробування, проведені з боєприпасами 7,62×51, показали високу балістичну стійкість цієї захисної конструкції, яку не було перфоровано. Лише незначне проникнення та часткові руйнування відбулися виключно в поверхневому шарі ММК. Ані на межі з металом основи, ні всередині пластини Ti–6Al–4V не виявлено слідів пластичної деформації, що свідчить про те, що всю енергію удару кулі було поглинуто шаром ММК. На підставі досліджень тонкої структури та текстури межі поділу між шарами було зроблено обґрунтоване припущення, що хвилеподібна геометрія межі між ними забезпечує додаткове відхилення та розсіяння хвиль, що виникають під час удару. Через порівняння результатів балістичних випробувань різних металевих матеріялів було зроблено висновок, що 3*D*-друкований двошаровий матеріал, який складається з верхнього шару Ti–6Al–4V + 40% TiC і базового шару Ti–6Al–4V, має незаперечну балістичну перевагу під час тестування набоями цього типу.

Ключові слова: адитивне виробництво, 3*D*-друк, титанові стопи, металоматричний композит, мікроструктура, текстура, балістичні характеристики.